Competing lattice instability and magnetism on the surface of kagome metals

Hengxin Tan ●* and Binghai Yan ●†

Department of Condensed Matter Physics, Weizmann Institute of Science, Rehovot 7610001, Israel

Only a few magnetic kagome materials exhibit lattice instabilities among the large kagome material array. In this work, we find that kagome magnets RMn$_6$Sn$_6$ (R = rare-earth elements) and their nonmagnetic counterparts RV$_6$Sn$_6$ exhibit an intriguing interplay between magnetism and lattice dynamics on their surfaces. Notably, RV$_6$Sn$_6$ surfaces terminated by kagome layers demonstrate pronounced lattice instabilities, manifesting as $\sqrt{3} \times \sqrt{3}$ and 2×2 surface charge orders (SCOs). These instabilities are absent on corresponding magnetic materials RMn$_6$Sn$_6$. Here, the SCO is suppressed by magnetism. Otherwise, surface distortions would significantly reduce the spin polarization, elevating the energy via Hund's rule. Thus, SCOs are energetically unfavorable on magnetic surfaces. The competition of magnetism and lattice instability is further substantiated by observing SCOs on V-substituted RMn$_6$Sn$_6$ kagome surfaces, contrasting with their absence on Mn-substituted RV$_6$Sn$_6$ surfaces. Our findings reveal unexpected surface instability and profound spin-lattice coupling in these kagome magnets, highlighting the complex dynamics hidden within magnetic materials.

I. INTRODUCTION

Kagome materials, characterized by a corner-sharing triangular sublattice, are a fertile playground for various correlated electronic orders [1–4]. The discovery of charge density wave (CDW) in nonmagnetic kagome superconductors [5–9] sparked immediate interest because of its close relationship with the potential time-reversal symmetry breaking and superconductivity. In contrast, magnetic kagome materials showing CDW are rare, primarily due to the lack of lattice instability in most systems and the competition between magnetism and other low-energy scale orders.

The recent discovery of CDW in the magnetic kagome metal FeGe [10] highlights the intricate interplay between magnetism and lattice instability [11–14], enabling the exploration of intertwining between these orders. This FeGe-type structure is derived by excluding the R element from the extensively studied magnetic kagome compounds RMn$_6$Sn$_6$ (R = Y, Gd-Lu) [15–25], where no charge instability has been reported. This structural resemblance raises the possibility of an underlying lattice instability in RMn$_6$Sn$_6$, potentially suppressed by magnetism and observable when magnetism is diminished. The observation of CDW transition in the nonmagnetic ScV$_6$Sn$_6$ [26–29], as opposed to its magnetic counterpart ScMn$_6$Sn$_6$ without CDW, suggests such a potential. However, the absence of CDW in other nonmagnetic RV$_6$Sn$_6$ variants underscores the complexity of these materials. This complexity prompts questions about the existence of competition between lattice instability and magnetism and its manifestation in the wider range. Our recent scanning tunneling microscopy (STM) studies reveal significant distortions on the surface of ScV$_6$Sn$_6$ [30], hinting at the possibility of observing this competition in a decreased dimension.

In this study, we elucidate the interplay between lattice instabilities and magnetism in surfaces of RV$_6$Sn$_6$ and RMn$_6$Sn$_6$. We reveal that the kagome layer on RV$_6$Sn$_6$ surfaces inherently exhibits charge instabilities, manifesting as $\sqrt{3} \times \sqrt{3}$ and 2×2 surface charge orders (SCOs), driven by phonon softening and characterized by distinct V trimer and cloverlike distortions. Introducing magnetic Mn in place of nonmagnetic V on these kagome surfaces leads to a significant weakening of Mn spin polarization due to surface distortions, increasing the magnetic energy via Hund's rule. This energy increase suppresses SCOs, further evidenced by the absence of SCOs in magnetic RMn$_6$Sn$_6$. Remarkably, substituting Mn with V on RMn$_6$Sn$_6$ kagome surfaces allows SCOs to reappear, underlining a potent competition between surface lattice instability and magnetism and highlighting a pathway to potential high-temperature SCOs. Our findings unveil complex dynamics in surfaces of kagome magnets and beyond.

II. RESULTS AND DISCUSSIONS

Bulk properties of RV$_6$Sn$_6$. The crystalline structure of RV$_6$Sn$_6$ comprises a Sn honeycomb layer, a RSn triangular layer, and two V-Sn kagome layers in a buckled configuration, as shown in Fig. 1(a). Prior experimental observations have identified a complex ordering of the R $4f$ magnetic moments below ~4 K [31–34]. Angle-resolved photoemission spectroscopy (ARPES) analysis has revealed the minimal influence of the $4f$ magnetism on the low-energy physics [35–37]. Our calculations demonstrate robust SCOs not only in the ferromagnetic TbV$_6$Sn$_6$, but also in paramagnetic GdV$_6$Sn$_6$ and nonmagnetic YV$_6$Sn$_6$. Consequently, we will omit discussions regarding f-electron magnetism. Given the
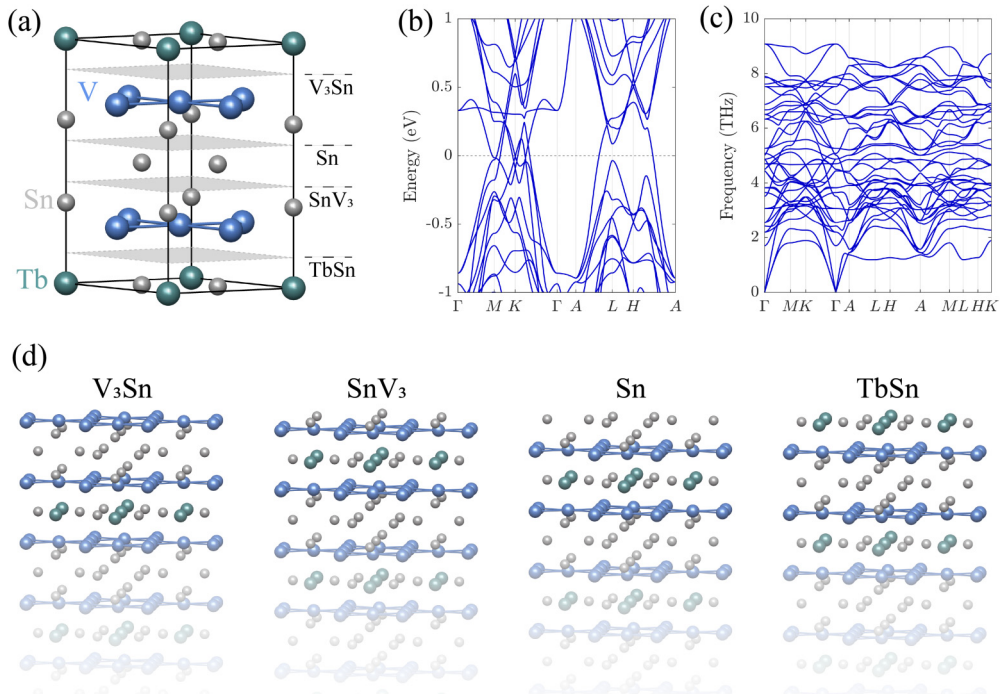
*hengxin.tan@weizmann.ac.il
†binghai.yan@weizmann.ac.il

195428-1

FIG. 1. Bulk properties of TbV$_6$Sn$_6$ and surface configurations. (a) The bulk crystal structure of TbV$_6$Sn$_6$. Grey planes stand for cleaving planes which generate four different terminations as labeled. (b) Bulk band structure without spin-orbital coupling. (c) Bulk phonon dispersion. (d) Four free-cleaved terminations. Both V$_3$Sn and SnV$_3$ are referred to as kagome surfaces. Notice that the surface V-kagome sublattice in the V$_3$Sn termination goes spontaneously below the highest Sn sublattice after surface relaxation.

similarity of results across all RV$_6$Sn$_6$ compounds, we will primarily illustrate our findings with TbV$_6$Sn$_6$.

The bulk band structure of TbV$_6$Sn$_6$ is depicted in Fig. 1(b), characterized by typical kagome band features, such as van Hove singularities at M/L, Dirac points at K/H, and a flat band at approximately 0.3 eV. Notice that all RV$_6$Sn$_6$ materials exhibit similar band structures [27,35,36,38,39]. In Fig. 1(c), the phonon spectrum of TbV$_6$Sn$_6$ confirms its bulk dynamical stability by showing the absence of imaginary phonon modes. This absence extends to all RV$_6$Sn$_6$ compounds (except for ScV$_6$Sn$_6$ [27]), indicating all RV$_6$Sn$_6$ compounds (except for Sc) are stable in their bulk forms. It is worth noting that among these stable compounds, LuV$_6$Sn$_6$ exhibits the softest phonon branch on the k_z plane, which may suggest its susceptibility to structural phase transitions under external influences such as strain (see the Supplemental Material, Sec. II A [40], for additional details).

SCOs of RV$_6$Sn$_6$. The layered structure of RV$_6$Sn$_6$ promises four different terminations, i.e., the RSn triangular surface, Sn honeycomb surface, and two kagome surfaces, V$_3$Sn and SnV$_3$, as shown in Figs. 1(a)–1(d). These different surfaces have been observed in various experiments [17,21,30,32,35,36]. The primary differentiation between the two kagome surfaces arises from the respective chemical configurations underneath. In the V$_3$Sn termination, the V-kagome sublattice is positioned above the closely associated Sn sublattice from the same buckled V-Sn layer, with the subsequent layer being the Sn honeycomb layer [41]. In contrast, the SnV$_3$ termination situates the V-kagome sublattice below the closely associated Sn sublattice, with the next layer the

RSn triangular layer. Both terminations show similar SCOs and are collectively called kagome surfaces within this work.

Figures 2(a)–2(d) display the surface phonon band structures of the four different terminations of TbV$_6$Sn$_6$, obtained from thick slab model calculations. Notably, the V$_3$Sn surface exhibits imaginary phonon modes across the entire surface Brillouin zone [Fig. 2(a)]. The interpretation of these modes unfolds as follows: (i) The imaginary phonon at Γ results in a 1×1 surface modulation, primarily involving the surface V layer trimerization [Fig. 2(e)]. This modulation reduces the surface's rotational symmetry from sixfold to threefold, while preserving the translational symmetry. However, such a trimerized surface is marked by a significant imaginary phonon at the K point (see the Supplemental Material, Sec. II C [40]), indicating its instability. (ii) The imaginary phonon at K induces a $\sqrt{3} \times \sqrt{3}$ SCO, as depicted in Fig. 2(f). In this phase with broken translational symmetry, the surface V-kagome layer transforms into a cloverlike pattern, resulting in a total energy decrease of about 307 meV per surface primitive unit cell (u.c.), relative to the pristine surface (see Table I). (iii) The imaginary phonon at M drives a 2×2 SCO, combining V trimers and clovers, as illustrated in Fig. 2(g). This phase exhibits a lower total energy of -394 meV/u.c. The dynamical stability of these two SCOs is confirmed by the absence of imaginary phonon modes in their respective phonon spectra (see the Supplemental Material, Sec. II C [40]). Typical scanning tunneling microscopy (STM) images at the charge neutral point are presented in Figs. 2(h)–2(j) with additional results available in the Supplemental Material, Sec. II H [40].
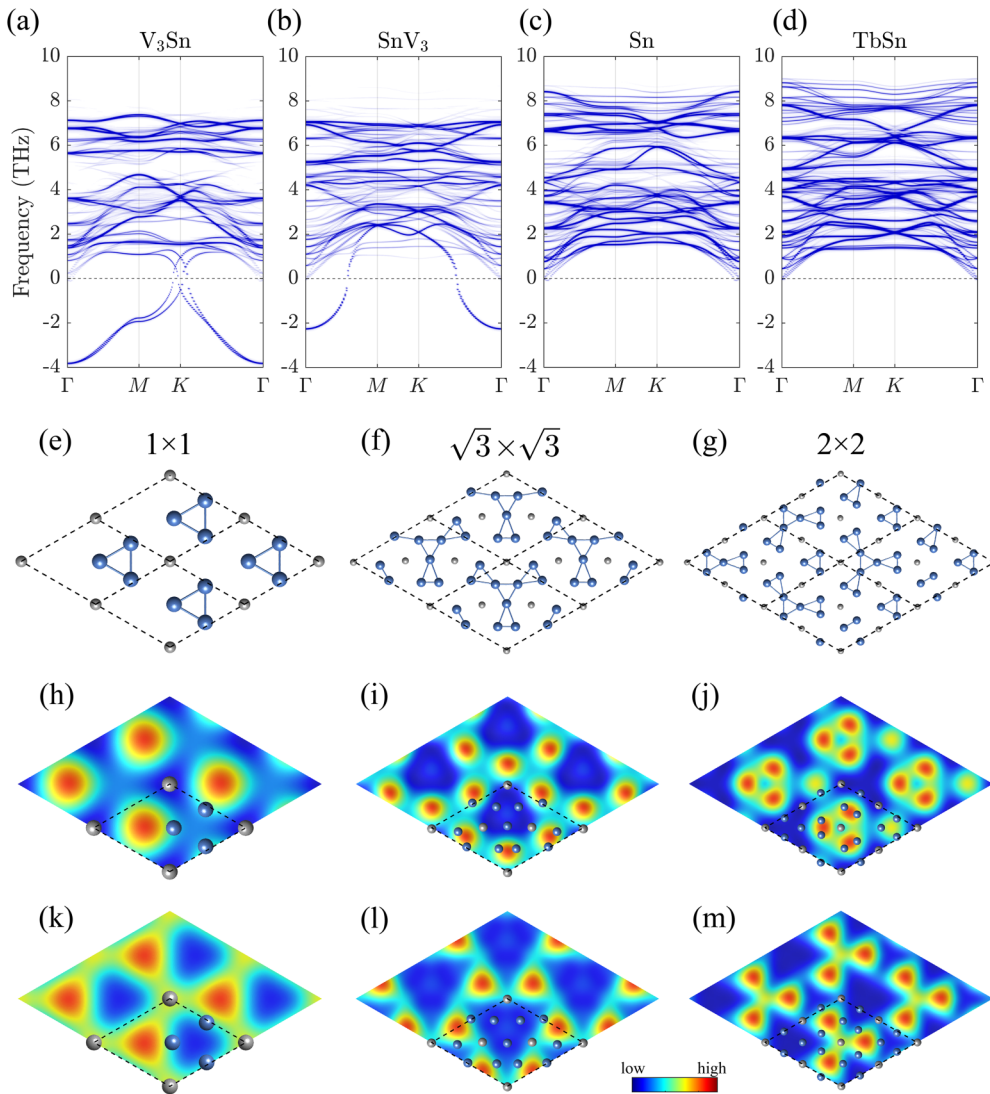
FIG. 2. SCOs of TbV_6Sn_6. (a)–(d) Surface phonon spectra of different terminations derived by projecting the phonon dispersions from four-unit-cell-thick slabs onto the surface layers. Negative frequencies signify imaginary phonon modes. (e)–(g) The Γ, K, M imaginary phonon mode-driven distortions in the V_3Sn surface: (e) 1×1 V trimerization, (f) $\sqrt{3} \times \sqrt{3}$ SCO (cloverlike pattern), (g) 2×2 SCO (mixed V trimer and clover). For clarity, only the topmost V and Sn sublattices are depicted in (e)–(g) for simplicity, with dashed diamonds denoting the smallest periodic cells. The $\sqrt{3} \times \sqrt{3}$ and 2×2 SCOs are also stable in the SnV_3 surface, despite the absence of imaginary phonons at M and K in (b). (h)–(j) STM images for 1×1, $\sqrt{3} \times \sqrt{3}$, and 2×2 SCOs, respectively, in the V_3Sn surface at the charge neutral point. (k)–(m) Analogous STM images for the SnV_3 surface.

In Fig. 2(b), the phonon spectrum of the SnV_3 termination reveals exclusively imaginary phonons at the Γ point. The Γ imaginary phonon instigates the 1×1 surface modulation with V trimers, as illustrated in Fig. 2(e), which reduces the total energy by -17 meV/u.c. Intriguingly, such a V-trimerized SnV_3 surface shows a substantial imaginary phonon at K, akin to the scenario in V_3Sn, as detailed in the Supplemental Material, Sec. II C [40]. Furthermore, the $\sqrt{3} \times \sqrt{3}$ and 2×2 SCOs displayed in Figs. 2(f) and 2(g) elicit more pronounced reductions in the total energy of the SnV_3 surface, amounting to -26 and -21 meV/u.c., respectively. An insightful deduction from the phonon band structure is that an imaginary phonon mode at a reciprocal space momentum generally implies the presence of a stable structure modulated by the same momentum. The SnV_3 surface, however, presents a paradoxical case by revealing the absence of a stable structure modulated by the Γ imaginary phonon and the unexpected emergence of energy-favored structures driven by the non-imaginary phonons at M/K. This peculiarity might arise from the effective screening of the long-range Γ imaginary phonon to the short-range M/K imaginary phonons, which manifests only after the elimination of the Γ imaginary phonon. Notably, this Γ imaginary phonon screening effect may also apply to the V_3Sn surface, exhibiting strong imaginary phonons at Γ and weak ones at M/K. STM images of SCOs for the SnV_3 surface at the charge neutral point are presented in Figs. 2(k)–2(m), with additional details available in the Supplemental Material, Sec. II H [40].

The phonon spectra of the Sn and TbSn terminations in Figs. 2(c) and 2(d) notably lack any soft modes. The

TABLE I. Total energy of SCOs on kagome terminations of $R\mathrm{V}_6\mathrm{Sn}_6$. The energy, with respect to the pristine termination, is in the unit of meV/u.c. (u.c. = surface primitive unit cell). Notice that the italicized 1×1 distortions are confirmed to show imaginary phonon modes at the K point. The 2×2 SCO in the SnV_3 termination of other R materials (except for Gd and Tb) and the $\sqrt{3} \times \sqrt{3}$ SCO in the SnV_3 termination of $\mathrm{ScV}_6\mathrm{Sn}_6$ go back to the 1×1 surface V trimerization after structural relaxation, indicating their instability. Sc and Sc* stand for the bulk pristine and $\sqrt{3} \times \sqrt{3} \times 3$ CDW phase, respectively.

	$\mathrm{V}_3\mathrm{Sn}$			SnV_3		
R	$\sqrt{3} \times \sqrt{3}$	2×2	1×1	$\sqrt{3} \times \sqrt{3}$	2×2	1×1
Gd	−318	−402	−214	−36	−33	−26
Tb	−307	−394	*−212*	−26	−21	*−17*
Dy	−304	−392	−204	−31	Unstable	−25
Ho	−300	−391	−200	−28	Unstable	−23
Er	−297	−388	−196	−25	Unstable	−22
Tm	−294	−386	−192	−22	Unstable	−21
Lu	−289	−383	−186	−17	Unstable	−16
Y	−305	−393	*−205*	−33	Unstable	*−27*
Sc	−251	−359	−155	Unstable	Unstable	−4
Sc*	−94			Unstable		

above-established SCOs in kagome terminations are also confirmed to be unstable on both surfaces. It is crucial to emphasize that these two surfaces can be achieved by overlaying one Sn (TbSn) layer atop the SnV_3 ($\mathrm{V}_3\mathrm{Sn}$) surface. Consequently, introducing additional layers effectively mitigates the instabilities observed in the kagome surfaces. This comparison underscores the pivotal role of exposing the kagome layer at the surface in attaining SCOs in $R\mathrm{V}_6\mathrm{Sn}_6$. Furthermore, it is worth noting that there are numerous flat phonon bands evident across all surfaces, which could potentially influence the phonon dynamics, as discussed in [42].

We apply the above SCOs to the kagome terminations of all other $R\mathrm{V}_6\mathrm{Sn}_6$. After adequate surface relaxation, these SCOs consistently reduce the total energy, as summarized in Table I. Similar to the Tb compound, the 2×2 SCO consistently exhibits a lower total energy in the $\mathrm{V}_3\mathrm{Sn}$ termination, while the $\sqrt{3} \times \sqrt{3}$ SCO attains a lower total energy in the SnV_3 termination across all R compounds. Remarkably, while the 2×2 SCO can be achieved in the SnV_3 termination of $\mathrm{GdV}_6\mathrm{Sn}_6$ following surface relaxation, the 2×2 distorted SnV_3 surfaces of Y and Dy-Lu materials spontaneously revert to the 1×1 trimerized surface configuration after relaxation, effectively restoring the broken translational symmetry. Phonon calculations additionally reveal that the 1×1 trimerized kagome surfaces of $\mathrm{YV}_6\mathrm{Sn}_6$ exhibit a pronounced imaginary phonon at K (resulting in the $\sqrt{3} \times \sqrt{3}$ SCO), notwithstanding the pristine SnV_3 surface of the Y compound only manifesting an imaginary phonon at the Γ point (elaborated in the Supplemental Material, Sec. II D [40]). Given the resemblance of these materials, we conjecture that the 1×1 trimerized kagome surfaces exhibit instability across all $R\mathrm{V}_6\mathrm{Sn}_6$ compounds (except for Sc). However, their total energies are included in Table I for reference and comparative analysis. These SCOs are pure surface effects, which are robust against
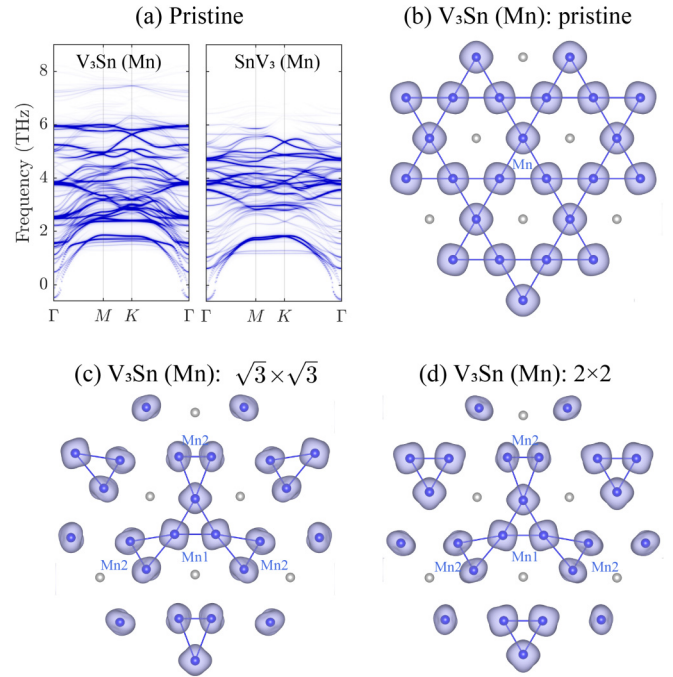

FIG. 3. Phonon and magnetization density of Mn-doped kagome surfaces of $\mathrm{TbV}_6\mathrm{Sn}_6$. (a) Phonon dispersions of two pristine surfaces, where Mn replaces the topmost V layer. The faint soft feature is caused by the calculation accuracy. (b) The magnetization density of the Mn-replaced pristine $\mathrm{V}_3\mathrm{Sn}$ surface, where the isosurface is $0.015\,e/\text{Å}^3$. (c),(d) Similar to (b), but with frozen SCOs, where Mn2 atoms (blue) have a smaller magnetization density area, indicating their weaker spin polarization.

the slab thickness, as comprehensively elucidated in the Supplemental Material, Sec. II E [40].

We have also extended our analysis of SCOs to the extensively studied $\mathrm{ScV}_6\mathrm{Sn}_6$. In the pristine bulk phase, while two SCOs reduce the energy of the $\mathrm{V}_3\mathrm{Sn}$ termination, they are unstable in the SnV_3 termination, and only the 1×1 surface trimerization reduces the total energy. This phenomenon may be attributed to the significantly higher in-plane chemical pressure in $\mathrm{ScV}_6\mathrm{Sn}_6$ (see the Supplemental Material, Sec. II A [40]). Furthermore, we applied the $\sqrt{3} \times \sqrt{3}$ SCO to kagome terminations of $\mathrm{ScV}_6\mathrm{Sn}_6$ in a bulk $\sqrt{3} \times \sqrt{3} \times 3$ CDW phase [26], and found it to be only stabilized in the $\mathrm{V}_3\mathrm{Sn}$ termination (Table I).

Suppression of SCO by magnetism. Now we explore the impact of magnetism on SCOs by substituting the outermost V kagome layer on $\mathrm{TbV}_6\mathrm{Sn}_6$ kagome terminations with a magnetic Mn kagome layer. Calculations indicate that the local magnetic moments of Mn form a ferromagnetic ordering. This magnetic substitution leads to the disappearance of SCOs, following sufficient surface relaxation. Indeed, such Mn-doped surfaces with frozen SCOs show much higher total energies (Table II). Moreover, phonon spectra analyses of these Mn-doped kagome surfaces reveal no lattice instabilities, as shown in Fig. 3(a). The interplay between SCOs and magnetism is further elucidated by studying magnetic counterpart $\mathrm{TbMn}_6\mathrm{Sn}_6$. Namely, the absence of imaginary phonon modes on kagome surfaces $\mathrm{Mn}_3\mathrm{Sn}$ and SnMn_3 indicates no

TABLE II. Properties of Mn-doped kagome surfaces of TbV_6Sn_6. The surface V kagome layer of TbV_6Sn_6 is replaced with Mn atoms where SCOs are frozen. "Up" and "dn" represent the spin-up and -down channels, respectively. Mn atoms are labeled in Figs. 3(b)–3(d). The first row of each surface shows the Bader charges (unit e); the second row displays the magnetization M (unit μ_B), which is equivalent to the difference between spin-up and -down Bader charges; the third row is the total energy δE relative to the pristine surface (eV per pristine cell, p.c.). The total charge of each Mn atom (spin-up + spin-down Bader charges) is nearly preserved by SCOs. SCOs transfer spin-up charges to the spin-down channel, leading to a decreased spin polarization (smaller magnetic moment).

Mn-replaced kagome surface		Pristine		$\sqrt{3} \times \sqrt{3}$ SCO				2×2 SCO			
		Mn up	Mn dn	Mn1 up	Mn1 dn	Mn2 up	Mn2 dn	Mn1 up	Mn1 dn	Mn2 up	Mn2 dn
V_3Sn	charge (e)	5.17	1.65	4.84	2.02	4.34	2.53	4.88	1.96	4.22	2.65
	M (μ_B)	3.52		2.82		1.81		2.92		1.57	
	δE (eV/p.c.)	0		1.23				1.29			
SnV_3	charge (e)	5.11	1.75	5.04	1.84	5.00	1.87	5.02	1.86	4.99	1.88
	M (μ_B)	3.36		3.20		3.13		3.16		3.11	
	δE (eV/p.c.)	0		0.38				0.54			

SCOs (see the Supplemental Material, Sec. II G [40]). Conversely, reintroducing V into kagome surfaces of $TbMn_6Sn_6$ stabilizes the SCOs. Notably, the cross substitution between V and Mn does not exert a noticeable strain effect, attributed to the similar effective radii of V and Mn ions (V 0.640 Å versus Mn 0.645 Å [43]). Thus, the stabilization or destabilization of SCOs in these kagome surfaces is more closely related to magnetic effects rather than mechanical strain. Notice that the f-electron magnetism of Tb does not affect SCOs.

These observations highlight the competition between lattice instabilities and magnetism. A detailed Bader charge analysis of Mn atoms of the Mn-doped kagome surfaces of TbV_6Sn_6 with frozen SCOs is presented in Table II. It shows that while the total charge of each Mn atom is preserved, SCOs transfer charges from the spin-up channel to the spin-down channel, weakening the spin polarization heavily. For example, on the Mn-doped V_3Sn surface, Mn atoms have initial spin-up/down charges of $5.17e/1.65e$, yielding a total charge of $6.82e$ and magnetization of $3.52\mu_B$. With the frozen $\sqrt{3} \times \sqrt{3}$ SCO, spin-up charges adjust to $4.84e$ (Mn1) and $4.34e$ [Mn2, labeled in Fig. 3(c)], and spin-down charges adjust to $2.02e$ (Mn1) and $2.53e$ (Mn2), nearly preserving total charges ($6.86e$ for Mn1, $6.87e$ for Mn2) but reducing magnetizations to $2.82\mu_B$ (Mn1) and $1.81\mu_B$ (Mn2). Magnetization densities are exemplified with Mn-doped V_3Sn in Figs. 3(b)–3(d), where the Mn2 atoms have a much smaller magnetization density area under SCOs. Similar behaviors are confirmed for all other surfaces and SCOs (changes are smaller in the SnV_3 surface because of its smaller SCO distortion amplitudes). Results of $TbMn_6Sn_6$ kagome terminations are found in the Supplemental Material, Sec. II G [40]. According to Hund's rule, which favors high-spin states in magnetic ions for maximum spin polarization, the reduction in spin polarization leads to increased magnetic energy, which outweighs the kinetic energy loss from structural distortions. As a result, the total energy of the surface is increased, mitigating surface distortions. For TbV_6Sn_6 and V-doped $TbMn_6Sn_6$ kagome terminations, the elimination of surface magnetism ceases its antagonistic effect on SCOs, resulting in SCOs as previously discussed.

This mechanism contrasts the scenario for the CDW formation of the kagome magnet FeGe. In FeGe, structural distortions lead to kinetic energy gains and increased spin polarization, reducing more magnetic energy [12–14]. Moreover, spin splitting shifts a von Hove singularity into the Fermi level in the spin minority band [11], enhancing Fermi surface nesting and promoting charge instability. The intricate interplay among spin, lattice, and charge degrees of freedom culminates in the CDW formation in FeGe and SCO suppression in RMn_6Sn_6, illustrating the complex quantum ground states emergent from the intertwined dynamics of these variables.

Now we address the potential experimental detection of the predicted SCOs. SCOs significantly disrupt the surface kagome layers, obfuscating certain surface states (see the Supplemental Material, Sec. II F [40]). ARPES appears as the initial experimental technique to consider. Notably, a limited number of ARPES experiments have been conducted on kagome terminations of RV_6Sn_6 [30,32,35–37,39]. While experiments observe some distinctive bands, ambiguous states are also present, whose origin remains challenging to identify. Consequently, the determination of the presence of SCOs in these experiments, as well as the characterization of their range (long range or short range), remains elusive. We propose that microscope techniques such as STM, capable of detecting local atomic structures, could be an optimal approach for SCO detection. Nevertheless, relatively few STM experiments have been conducted on RV_6Sn_6. In the case of ScV_6Sn_6 within the bulk $\sqrt{3} \times \sqrt{3} \times 3$ CDW phase, recent STM experiments on kagome terminations observed a prominent $\sqrt{3} \times \sqrt{3}$ reconstruction [30]. We do not conclude that it is the $\sqrt{3} \times \sqrt{3}$ SCO (Table I) because the bulk CDW also exhibits a $\sqrt{3} \times \sqrt{3}$ in-plane modulation. However, it is crucial to underscore that the bulk CDW of ScV_6Sn_6 exclusively involves Sc/Sn out-of-plane movements, with minimal distortion in the V kagome layer [26,27]. This contrasts with the STM experiment, underscoring the need for more comprehensive studies for RV_6Sn_6.

In the context of RMn_6Sn_6, intriguing phenomena are anticipated. It is noteworthy to consider the possibility of observing SCOs in RMn_6Sn_6 at high temperatures when the magnetic order ceases to exist. Confirmation of this phenomenon in experiments would establish RMn_6Sn_6 as a rare class of symmetry-descending materials when temperature increases [44]. We recommend more STM

experiments on $R\text{Mn}_6\text{Sn}_6$ at elevated temperatures to explore this intriguing prospect. Furthermore, the sizable structural distortion accompanying SCOs might also suggest the potential for a significant surface magnetostriction [45] and piezomagnetic effect, which would benefit the application of antiferromagnets.

III. CONCLUSION

In conclusion, we have revealed the pervasive $\sqrt{3} \times \sqrt{3}$ and 2×2 SCOs across kagome terminations in $R\text{V}_6\text{Sn}_6$, which are suppressed in $R\text{Mn}_6\text{Sn}_6$ by magnetism due to the profound competition between lattice instability and magnetism through Hund's rule. We call for additional experimental efforts to explore these fascinating surface phenomena. Our findings suggest the existence of undiscovered quantum states in general magnets, potentially accessible through the suppression of magnetism.

ACKNOWLEDGMENTS

[1] J. Wen, A. Rüegg, C.-C. Joseph Wang, and G. A. Fiete, Interaction-driven topological insulators on the kagome and the decorated honeycomb lattices, Phys. Rev. B **82**, 075125 (2010).

[2] M. L. Kiesel and R. Thomale, Sublattice interference in the kagome Hubbard model, Phys. Rev. B **86**, 121105(R) (2012).

[3] W.-S. Wang, Z.-Z. Li, Y.-Y. Xiang, and Q.-H. Wang, Competing electronic orders on kagome lattices at van Hove filling, Phys. Rev. B **87**, 115135 (2013).

[4] M. L. Kiesel, C. Platt, and R. Thomale, Unconventional Fermi surface instabilities in the kagome Hubbard model, Phys. Rev. Lett. **110**, 126405 (2013).

[5] B. R. Ortiz, S. M. L. Teicher, Y. Hu, J. L. Zuo, P. M. Sarte, E. C. Schueller, A. M. M. Abeykoon, M. J. Krogstad, S. Rosenkranz, R. Osborn, R. Seshadri, L. Balents, J. He, and S. D. Wilson, CsV$_3$Sb$_5$: A $\mathbb{Z}_2$ topological kagome metal with a superconducting ground state, Phys. Rev. Lett. **125**, 247002 (2020).

[6] Y.-X. Jiang, J.-X. Yin, M. M. Denner, N. Shumiya, B. R. Ortiz, G. Xu, Z. Guguchia, J. He, M. S. Hossain, X. Liu *et al.*, Unconventional chiral charge order in kagome superconductor KV$_3$Sb$_5$, Nat. Mater. **20**, 1353 (2021).

[7] H. Tan, Y. Liu, Z. Wang, and B. Yan, Charge density waves and electronic properties of superconducting kagome metals, Phys. Rev. Lett. **127**, 046401 (2021).

[8] Z. Liang, X. Hou, F. Zhang, W. Ma, P. Wu, Z. Zhang, F. Yu, J.-J. Ying, K. Jiang, L. Shan, Z. Wang, and X.-H. Chen, Three-dimensional charge density wave and surface-dependent vortex-core states in a Kagome superconductor CsV$_3$Sb$_5$, Phys. Rev. X **11**, 031026 (2021).

[9] H. Chen, H. Yang, B. Hu, Z. Zhao, J. Yuan, Y. Xing, G. Qian, Z. Huang, G. Li, Y. Ye *et al.*, Roton pair density wave in a strong-coupling kagome superconductor, Nature (London) **599**, 222 (2021).

[10] X. Teng, L. Chen, F. Ye, E. Rosenberg, Z. Liu, J.-X. Yin, Y.-X. Jiang, J. S. Oh, M. Z. Hasan, K. J. Neubauer *et al.*, Discovery of charge density wave in a kagome lattice antiferromagnet, Nature (London) **609**, 490 (2022).

[11] X. Teng, J. S. Oh, H. Tan, L. Chen, J. Huang, B. Gao, J.-X. Yin, J.-H. Chu, M. Hashimoto, D. Lu *et al.*, Magnetism and charge density wave order in kagome FeGe, Nat. Phys. **19**, 814 (2023).

[12] H. Miao, T. T. Zhang, H. X. Li, G. Fabbris, A. H. Said, R. Tartaglia, T. Yilmaz, E. Vescovo, J-X Yin, S. Murakami *et al.*, Signature of spin-phonon coupling driven charge den-sity wave in a kagome magnet, Nat. Commun. **14**, 6183 (2023).

[13] Y. Wang, Enhanced spin-polarization via partial Ge-dimerization as the driving force of the charge density wave in FeGe, Phys. Rev. Mater. **7**, 104006 (2023).

[14] Z. Chen, X. Wu, S. Zhou, J. Zhang, R. Yin, Y. Li, M. Li, J. Gong, M. He, Y. Chai, X. Zhou, Y. Wang, A. Wang, Y.-J. Yan, and D.-L. Feng, Long-ranged charge order conspired by magnetism and lattice in an antiferromagnetic kagome metal, arXiv:2307.07990.

[15] N. J. Ghimire, R. L. Dally, L. Poudel, D. C. Jones, D. Michel, N. T. Magar, M. Bleuel, M. A. McGuire, J. S. Jiang, J. F. Mitchell, J. W. Lynn, and I. I. Mazin, Competing magnetic phases and fluctuation-driven scalar spin chirality in the kagome metal YMn$_6$Sn$_6$, Sci. Adv. **6**, eabe2680 (2020).

[16] S. X. M. Riberolles, T. J. Slade, D. L. Abernathy, G. E. Granroth, B. Li, Y. Lee, P. C. Canfield, B. G. Ueland, L. Ke, and R. J. McQueeney, Low-temperature competing magnetic energy scales in the topological ferrimagnet TbMn$_6$Sn$_6$, Phys. Rev. X **12**, 021043 (2022).

[17] J.-X. Yin, W. Ma, T. A. Cochran, X. Xu, S. S. Zhang, H.-J. Tien, N. Shumiya, G. Cheng, K. Jiang, B. Lian, Z. Song, G. Chang, I. Belopolski, D. Multer, M. Litskevich, Z.-J. Cheng, X. P. Yang, B. Swidler, H. Zhou, H. Lin *et al.*, Quantum-limit Chern topological magnetism in TbMn$_6$Sn$_6$, Nature (London) **583**, 533 (2020).

[18] H. Zhang, X. Feng, T. Heitmann, A. I. Kolesnikov, M. B. Stone, Y.-M. Lu, and X. Ke, Topological magnon bands in a room-temperature kagome magnet, Phys. Rev. B **101**, 100405(R) (2020).

[19] M. Li, Q. Wang, G. Wang, Z. Yuan, W. Song, R. Lou, Z. Liu, Y. Huang, Z. Liu, H. Lei *et al.*, Dirac cone, flat band and saddle point in kagome magnet YMn$_6$Sn$_6$, Nat. Commun. **12**, 3129 (2021).

[20] X. Xu, J.-X. Yin, W. Ma, H.-J. Tien, X.-B. Qiang, P. V. Reddy, H. Zhou, J. Shen, H.-Z. Lu, T.-R. Chang *et al.*, Topological charge-entropy scaling in kagome Chern magnet TbMn$_6$Sn$_6$, Nat. Commun. **13**, 1197 (2022).

[21] H. Li, H. Zhao, K. Jiang, Q. Wang, Q. Yin, N.-N. Zhao, K. Liu, Z. Wang, H. Lei, and I. Zeljkovic, Manipulation of Dirac band curvature and momentum-dependent g factor in a kagome magnet, Nat. Phys. **18**, 644 (2022).

[22] T. Asaba, S. M. Thomas, M. Curtis, J. D. Thompson, E. D. Bauer, and F. Ronning, Anomalous Hall effect in the kagome ferrimagnet GdMn$_6$Sn$_6$, Phys. Rev. B **101**, 174415 (2020).

[23] W. Ma, X. Xu, J.-X. Yin, H. Yang, H. Zhou, Z.-J. Cheng, Y. Huang, Z. Qu, F. Wang, M. Z. Hasan, and S. Jia, Rare earth engineering in RMn$_6$Sn$_6$ (R = Gd-Tm, Lu) topological kagome magnets, Phys. Rev. Lett. **126**, 246602 (2021).

[24] L. Gao, S. Shen, Q. Wang, W. Shi, Y. Zhao, C. Li, W. Cao, C. Pei, J.-Y. Ge, G. Li, J. Li, Y. Chen, S. Yan, and Y. Qi, Anomalous Hall effect in ferrimagnetic metal RMn$_6$Sn$_6$ (R = Tb, Dy, Ho) with clean Mn kagome lattice, Appl. Phys. Lett. **119**, 092405 (2021).

[25] H. Zhang, J. Koo, C. Xu, M. Sretenovic, B. Yan, and X. Ke, Exchange-biased topological transverse thermoelectric effects in a kagome ferrimagnet, Nat. Commun. **13**, 1091 (2022).

[26] Hasitha W. Suriya Arachchige, William R. Meier, M. Marshall, T. Matsuoka, R. Xue, M. A. McGuire, R. P. Hermann, H. Cao, and D. Mandrus, Charge density wave in kagome lattice intermetallic ScV$_6$Sn$_6$, Phys. Rev. Lett. **129**, 216402 (2022).

[27] H. Tan and B. Yan, Abundant lattice instability in kagome metal ScV$_6$Sn$_6$, Phys. Rev. Lett. **130**, 266402 (2023).

[28] S. Cao, C. Xu, H. Fukui, T. Manjo, M. Shi, Y. Liu, C. Cao, and Y. Song, Competing charge-density wave instabilities in the kagome metal ScV$_6$Sn$_6$, Nat. Commun. **14**, 7671 (2023).

[29] A. Korshunov, H. Hu, D. Subires, Y. Jiang, D. Călugăru, X. Feng, A. Rajapitamahuni, C. Yi, S. Roychowdhury, M. G. Vergniory, J. Strempfer, C. Shekhar, E. Vescovo, D. Chernyshov, A. H. Said, A. Bosak, C. Felser, B. A. Bernevig, and S. Blanco-Canosa, Softening of a flat phonon mode in the kagome ScV$_6$Sn$_6$, Nat. Commun. **14**, 6646 (2023).

[30] S. Cheng, Z. Ren, H. Li, J. Oh, H. Tan, G. Pokharel, J. M. DeStefano, E. Rosenberg, Y. Guo, Y. Zhang, Z. Yue, Y. Lee, S. Gorovikov, M. Zonno, M. Hashimoto, D. Lu, L. Ke, F. Mazzola, J. Kono, R. J. Birgeneau *et al.*, Nanoscale visualization and spectral fingerprints of the charge order in ScV$_6$Sn$_6$ distinct from other kagome metals, npj Quantum Mater. **9**, 14 (2024).

[31] G. Pokharel, B. Ortiz, J. Chamorro, P. Sarte, L. Kautzsch, G. Wu, J. Ruff, and S. D. Wilson, Highly anisotropic magnetism in the vanadium-based kagome metal TbV$_6$Sn$_6$, Phys. Rev. Mater. **6**, 104202 (2022).

[32] E. Rosenberg, J. M. DeStefano, Y. Guo, J. S. Oh, M. Hashimoto, D. Lu, R. J. Birgeneau, Y. Lee, L. Ke, M. Yi, and J.-H. Chu, Uniaxial ferromagnetism in the kagome metal TbV$_6$Sn$_6$, Phys. Rev. B **106**, 115139 (2022).

[33] X. Zhang, Z. Liu, Q. Cui, Q. Guo, N. Wang, L. Shi, H. Zhang, W. Wang, X. Dong, J. Sun, Z. Dun, and J. Cheng, Electronic and magnetic properties of intermetallic kagome magnets RV$_6$Sn$_6$(R = Tb-Tm), Phys. Rev. Mater. **6**, 105001 (2022).

[34] J. Lee and E. Mun, Anisotropic magnetic property of single crystals RV$_6$Sn$_6$(R = Y, Gd-Tm, Lu), Phys. Rev. Mater. **6**, 083401 (2022).

[35] S. Peng, Y. Han, G. Pokharel, J. Shen, Z. Li, M. Hashimoto, D. Lu, B. R. Ortiz, Y. Luo, H. Li, M. Guo, B. Wang, S. Cui, Z. Sun, Z. Qiao, S. D. Wilson, and J. He, Realizing kagome band structure in two-dimensional kagome surface states of RV$_6$Sn$_6$ (R = Gd, Ho), Phys. Rev. Lett. **127**, 266401 (2021).

[36] Y. Hu, X. Wu, Y. Yang, S. Gao, N. C. Plumb, A. P. Schnyder, W. Xie, J. Ma, and M. Shi, Tunable topological Dirac surface states and van Hove singularities in kagome metal GdV$_6$Sn$_6$, Sci. Adv. **8**, eadd2024 (2022).

[37] D. D. Sante, C. Bigi, P. Eck, S. Enzner, A. Consiglio, G. Pokharel, P. Carrara, P. Orgiani, V. Polewczyk, J. Fujii, P. D. C. King, I. Vobornik, G. Rossi, I. Zeljkovic, S. D. Wilson, R. Thomale, G. Sangiovanni, G. Panaccione, and F. Mazzola, Flat band separation and robust spin berry curvature in bilayer kagome metals, Nat. Phys. **19**, 1135 (2023).

[38] G. Pokharel, S. M. L. Teicher, B. R. Ortiz, P. M. Sarte, G. Wu, S. Peng, J. He, R. Seshadri, and S. D. Wilson, Electronic properties of the topological kagome metals YV$_6$Sn$_6$ and GdV$_6$Sn$_6$, Phys. Rev. B **104**, 235139 (2021).

[39] J. Ding, N. Zhao, Z. Tao, Z. Huang, Z. Jiang, Y. Yang, S. Cho, Z. Liu, J. Liu, Y. Guo, K. Liu, Z. Liu, and D. Shen, Kagome surface states and weak electronic correlation in vanadium-kagome metals, J. Phys.: Condens. Matter **35**, 405502 (2023).

[40] See Supplemental Material at http://link.aps.org/supplemental/10.1103/PhysRevB.109.195428 for methods employed in our calculations and extended results and discussions about the bulk, surfaces, and thin films of TbV$_6$Sn$_6$ and YV$_6$Sn$_6$, and properties of magnetic kagome surfaces (Mn-doped TbV$_6$Sn$_6$, TbMn$_6$Sn$_6$ and V-doped TbMn$_6$Sn$_6$), which includes Refs. [26,27,32,36,46–53].

[41] After structural relaxation, the V-kagome sublattice goes below the closely associated Sn sublattice in the V$_3$Sn termination.

[42] H. Hu, Y. Jiang, D. Călugăru, X. Feng, D. Subires, M. G. Vergniory, C. Felser, S. Blanco-Canosa, and B. A. Bernevig, Kagome materials I: SG 191, ScV$_6$Sn$_6$. Flat phonon soft modes and unconventional CDW formation: Microscopic and effective theory, arXiv:2305.15469.

[43] R. D. Shannon and C. T. Prewitt, Effective ionic radii in oxides and fluorides, Acta Crystallogr. Sect. B **25**, 925 (1969).

[44] S. Wu, M. L. Klemm, J. Shah, E. T. Ritz, C. Duan, X. Teng, B. Gao, F. Ye, M. Matsuda, F. Li, X. Xu, M. Yi, T. Birol, P. Dai, and G. Blumberg, Symmetry breaking and ascending in the magnetic Kagome metal FeGe, Phys. Rev. X **14**, 011043 (2024).

[45] E. W. Lee, Magnetostriction and magnetomechanical effects, Rep. Prog. Phys. **18**, 184 (1955).

[46] G. Kresse and J. Furthmüller, Efficient iterative schemes for *ab initio* total-energy calculations using a plane-wave basis set, Phys. Rev. B **54**, 11169 (1996).

[47] G. Kresse and J. Furthmüller, Efficiency of *ab initio* total energy calculations for metals and semiconductors using a plane-wave basis set, Comput. Mater. Sci. **6**, 15 (1996).

[48] J. P. Perdew, K. Burke, and M. Ernzerhof, Generalized gradient approximation made simple, Phys. Rev. Lett. **77**, 3865 (1996).

[49] V. Wang, N. Xu, J.-C. Liu, G. Tang, and W.-T. Geng, VASPKIT: A user-friendly interface facilitating high-throughput computing and analysis using VASP code, Comput. Phys. Commun. **267**, 108033 (2021).

[50] A. Togo and I. Tanaka, First principles phonon calculations in materials science, Scr. Mater. **108**, 1 (2015).

[51] Y. Hu, J. Ma, Y. Li, Y. Jiang, D. J. Gawryluk, T. Hu, J. Teyssier, V. Multian, Z. Yin, S. Xu *et al.*, Phonon promoted charge density wave in topological kagome metal ScV$_6$Sn$_6$, Nat. Commun. **15**, 1658 (2024).

[52] H. Ishikawa, T. Yajima, M. Kawamura, H. Mitamura, and K. Kindo, GdV_6Sn_6: A multi-carrier metal with non-magnetic 3d-electron Kagome bands and 4f-electron magnetism, J. Phys. Soc. Jpn. **90**, 124704 (2021).

[53] L. Romaka, Y. Stadnyk, V.V. Romaka, P. Demchenko, M. Stadnyshyn, and M. Konyk, Peculiarities of component interaction in {Gd, Er}–V–Sn Ternary systems at 870 K and crystal structure of RV_6Sn_6 stannides, J. Alloys Compd. **509**, 8862 (2011).